Calculation of terahertz conductivity spectra in semiconductors with nanoscale modulation

Jan Mrozek and Hynek Němec*

Institute of Physics, Academy of Sciences of the Czech Republic, Na Slovance 2, 182 21 Prague 8, Czech Republic

(Received 26 April 2012; published 14 August 2012)

Monte Carlo simulations are employed to calculate terahertz conductivity of charge carriers in a potential with periodic modulation on the nanoscale. The modulation gives rise to two characteristic features in the conductivity spectra: a Drude peak owing to charge carriers with kinetic energy exceeding the modulation depth, and resonance due to charge carriers localized around potential minima. Both peaks shift in an applied magnetic field. We discuss the relationship between the modulation potential and the positions and strengths of the resonances. We also analyze the role of depolarization fields which are responsible for the difference between local and effective conductivity.

DOI: 10.1103/PhysRevB.86.075308 PACS number(s): 73.63.−b, 78.67.−n

I. INTRODUCTION

Terahertz (THz) conductivity spectra contain rich information on transport processes in semiconductors. This is apparent namely in bulk semiconductors, where the conductivity is frequently described by the simple Drude model[1]

$$\sigma_{\mathrm{Drude}}(f) = \frac{ne_0^2}{m}\frac{\tau_{\mathrm{D}}}{1-2\pi i f\tau_{\mathrm{D}}} \equiv ne_0\mu_{\mathrm{Drude}}(f), \qquad (1)$$

where e_0 is the positive elementary charge, n is the density of conducting charge carriers (either due to doping or generated by photoexcitation), m is their effective mass, τ_{D} is their momentum relaxation time, and $\mu_{\mathrm{Drude}}(f)$ is the frequency-dependent mobility. Since typical momentum relaxation times in semiconductors are of the order of 100 fs, the most pronounced dispersion occurs right in the THz range. Deviations of THz conductivity from the Drude behavior can indicate, for example, a distribution of relaxation times.[2,3]

While THz conductivity spectra of bulk semiconductors are well understood, this is not the case for nanostructured semiconductors (Ref. 4, and references therein). Nonhomogeneity of these materials gives rise to complex depolarization fields, which are responsible for a nontrivial relation between the macroscopic (effective) and local conductivity of semiconductor nanostructures.[4,5] But foremost, dimensions of nanoparticles are frequently comparable to the mean free path of charge carriers, which fundamentally affects transport of charge carriers, and in turn, the spectrum of their local conductivity.[6] However, the local conductivity was theoretically investigated only in a very limited set of model systems.

Spectra of various nanoparticulate systems have been frequently fitted[7–10] using the Drude-Smith model,[11] which is purely phenomenological and provides no microscopic insight into the underlying physical processes. It has also been criticized that it does not respect the time homogeneity, i.e., it assumes that the first scattering event is different from the others.[5] More detailed information was gained from Monte Carlo calculations of far-infrared mobility.[6] In particular, for the first time it became possible to quantify the relation between THz spectra and probabilities of electron transport between semiconductor nanoparticles. For example, comparison of these calculations with the measured spectra can be used for the determination of mean nanocrystal sizes.[12] Monte Carlo calculations also revealed the existence of two different length scales of charge localization in CdS nanocrystals attributed to the formation of clusters of nanocrystals.[13] It should be noted that the spectrum of such complex systems can never be described by the Drude-Smith model.

All the mentioned Monte Carlo calculations of far-infrared mobility have in common a probabilistic description of interparticle charge transport. This simplifying assumption has a good justification in disordered nanoparticulate systems: Instead of specifying the conductive coupling for each nanoparticle in a large ensemble, it is more useful to describe it by an average interparticle transition probability. On the other hand, such an assumption does not reflect a possible dependence of transition probability on carrier energy and it is not applicable in systems where no clear interfaces exist. A notable example is an artificial graphene where nanostructuring is achieved by a periodic modulation of the potential in which electrons move.[14]

THz conductivity spectra can be efficiently measured by time-resolved THz spectroscopy, which is a noncontact technique offering subpicosecond time resolution.[15] Together with a deep knowledge of local THz conductivity of model systems, time-resolved THz spectroscopy can become a powerful instrument for understanding charge transport in nanostructured networks down to the earliest times.[13,16]

In this paper, we analyze theoretically the far-infrared response of a three-dimensional electron gas in a potential periodically modulated on the nanoscale. We find that this response qualitatively differs from the conductivity of nanoparticulate systems with clear interfaces. We also investigate how the response of nanostructured semiconductors evolves with magnetic field. Finally, we analyze the role of depolarization fields. This step is essential for a direct comparison with experimental results which provide an effective conductivity, not the local one.

II. MONTE CARLO SIMULATION

The calculations are based on Monte Carlo simulations of the thermal motion of charge carriers in a modulated potential. The carrier motion is governed by classical Newton equations, which are solved by the fourth-order Runge-Kutta method. In addition, charge carriers are scattered with mean time τ_{s} corresponding to the mean momentum relaxation time

in the bulk material. Upon scattering, the velocity vector randomizes according to Maxwell-Boltzmann distribution. The calculated velocity autocorrelation function is then used for the determination of mobility of carriers by using the Kubo formula[6,17]

$$\mu_{ij}(f) = \frac{e_0}{k_B T} \int_0^\infty \langle v_i(0) v_j(t) \rangle e^{2\pi i f t}\, dt, \tag{2}$$

in which the averaging $\langle \ldots \rangle$ takes place over a canonical ensemble of carriers with temperature T.

The simulations are carried out for a set of charge carriers. Their initial positions are random and velocities follow the Maxwell-Boltzmann distribution. A thermalization phase follows (charge carriers are allowed to move according to the Newton equations and undergo the scattering): This ensures that the carriers reach a distribution close to thermal equilibrium. After this phase, the movement of charge carriers is recorded and the average $\langle \ldots \rangle$ in Eq. (2) is replaced by a time average. A typical integration range in Eq. (2) was 40 ps and about one million sequences were used to calculate the average.

Characteristics related to a modulation of the potential were first investigated for a one-dimensional periodic modulation. A prototype of a weak modulation is the sinusoidal potential

$$V(x) = -\frac{V_0}{2} \sin\left(\frac{2\pi x}{L}\right), \tag{3}$$

where V_0 is its depth and L is its period. In order to also study the impact of the shape of the potential, we employ a potential defined as

$$\begin{aligned} V(x) &= V_0 \frac{\upsilon(x) - \upsilon(0)}{\upsilon(L) - \upsilon(0)}, \\ \upsilon(x) &= \arctan\left[\gamma\left(\tfrac{x}{L} - \tfrac{\alpha}{2}\right)\right] - \arctan[\gamma(\tfrac{x}{L} + \tfrac{\alpha}{2})] \\ &\quad + \arctan\left[\gamma\left(\tfrac{x}{L}+1-\tfrac{\alpha}{2}\right)\right] - \arctan\left[\gamma\left(\tfrac{x}{L}-1+\tfrac{\alpha}{2}\right)\right] \end{aligned} \tag{4}$$

in the interval $(-L/2, L/2)$ and periodically extended [illustration follows in Fig. 4(a)]. This form allows for control of the relative width α of the potential bottom and the relative steepness γ of the potential walls. The response in these potentials is discussed in Sec. III A— the parameters employed for illustrations are selected with the aim of making the principal spectral characteristics clearly visible.

Finally, we examined response in a two-dimensional periodically modulated potential with hexagonal symmetry, which was recently employed for theoretical investigation of the band structure of artificial graphene:[18]

$$V(\mathbf{r}) = V_0[\cos\, \mathbf{g}_1\mathbf{r} + \cos\, \mathbf{g}_2\mathbf{r} + \cos(\mathbf{g}_1 - \mathbf{g}_2)\mathbf{r}], \tag{5}$$

where $\mathbf{g}_1 = 2\pi/L(1/\sqrt{3},1,0)$ and $\mathbf{g}_2 = 2\pi/L(2/\sqrt{3},0,0)$ are the basis vectors in the reciprocal space. In a magnetic field $\mathbf{B}$, the Lorentz force $-e_0\mathbf{v} \times \mathbf{B}$ additionally acts on charge carriers. Here we consider only the geometry where $\mathbf{B}$ is normal to the plane defined by the vectors $\mathbf{g}_1$ and $\mathbf{g}_2$. The response is analyzed in Sec. III B. In this case, parameters close to those employed in the experiments in Ref. 18 are used for illustrations.

We stress that all calculations carried out here are classical (they only employ the effective mass of charge carriers) and they do not account for any quantum phenomena. To estimate the possible limitations, we examine the energy levels $E_n = (nh/L)^2/(8m)$ in an infinitely deep quantum well. For example, a width $L = 100$ nm results in energy spacing $E_2 - E_1 = 0.038$ meV, which corresponds to temperature 0.44 K. This means that the classical limit should be sufficient for moderately low temperatures (e.g., above liquid helium temperature) and for not too strong confinement (characteristic dimensions exceeding 10 nm). Quantum-mechanical calculations are much more difficult; they were employed, for example, for calculation of the absorption cross section for electrons in InGaAs nanorods.[19]

III. DISCUSSION

A. Response without magnetic field

Figure 1(a) shows examples of charge trajectories in the potential (3) with various depths. For a low modulation depth ($V_0 \ll k_B T$), charge movement is governed by scattering events separated by nearly uniform motion only weakly perturbed by the modulation. For a deep modulation ($V_0 \gg k_B T$), charges cannot pass over potential barriers and they only oscillate near potential minima. For intermediate modulation depth ($V_0 \sim k_B T$), both these modes alternate, as the energy of charges changes upon scattering. All these regimes are

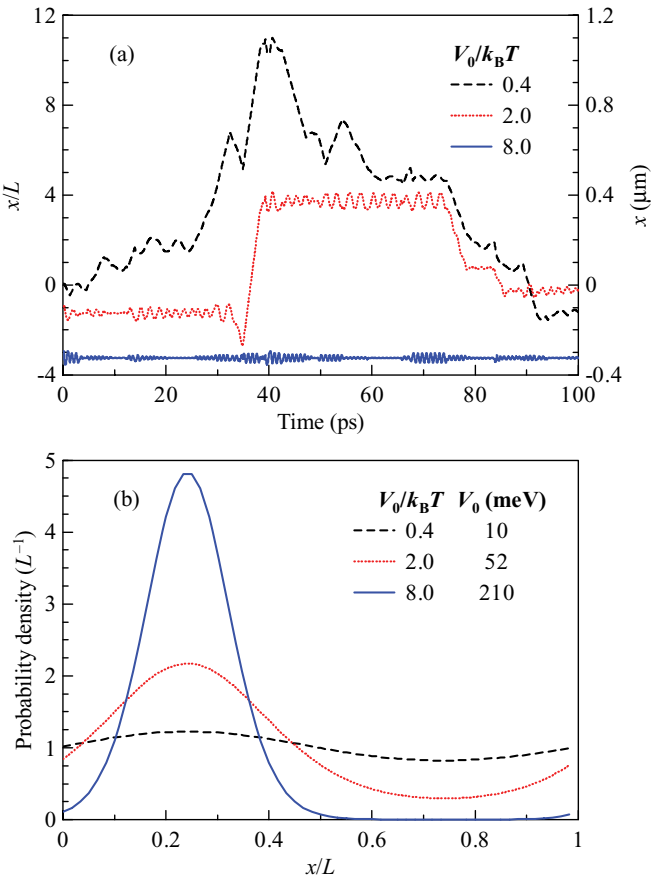

FIG. 1. (Color online) (a) Examples of trajectories of charges moving in the potential (3) with various depths. (b) Probability density of charges within one period of the potential. Calculation parameters: $L = 100$ nm, $\tau_s = 1$ ps, $m = m_e$, and $T = 300$ K.

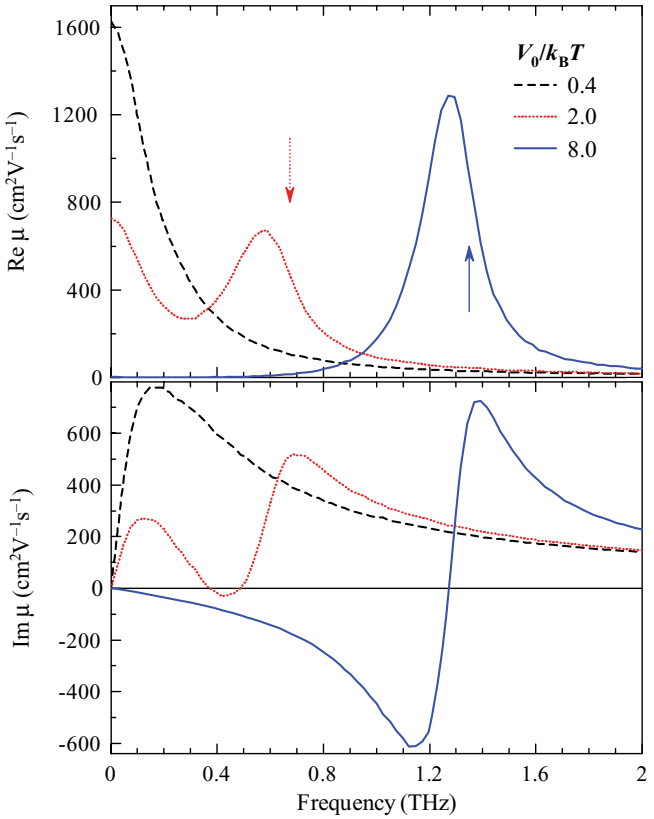

FIG. 2. (Color online) Real and imaginary part of mobility spectra of charges moving in potential (3) with various depths. The spectra were calculated with the same parameters as in Fig. 1. The arrows indicate frequencies calculated using Eq. (6).

characterized by different degrees of charge localization [Fig. 1(b)].

These considerations explain the related mobility spectra in Fig. 2. For the weak modulation, charges respond as if they were free and a Drude peak appears at zero frequency (its width is controlled by the scattering time τ_s). Conversely, for the strong modulation, charges oscillate around equilibrium positions, thus giving rise to an oscillator-like response.[20] For the intermediate depth, both Drude and oscillator peaks appear—their relative weights are controlled by the modulation depth. Such a behavior is qualitatively different from the response of charges in nanoparticles with semipermeable boundaries, which is characterized by a single broad peak.[6] The difference can be best understood in the limit of infinite scattering time. In a modulated potential, each charge is then either localized (it can never gain energy to pass over the potential maximum) or delocalized (its energy always exceeds the potential maximum), i.e., it has either Drude or oscillator response. Averaging over a canonical ensemble of charges then yields a superposition of the Drude and oscillator peaks. However, in the case of charges in nanoparticles, each charge (regardless of its energy) will interact with the nanoparticle boundary: Each trajectory will therefore contain a statistically identical mix of scattering and reflection events on the particle boundary. In turn, one finds a single broad peak in the mobility spectrum.[6]

When the potential is sufficiently deep so that most charges are close to the potential minima, the frequency of the oscillator response can be approximated by the oscillator frequency in the potential minimum

$$f_0 = \frac{1}{2\pi}\sqrt{\frac{1}{m}\left.\frac{\partial^2 V}{\partial x^2}\right|_{x:V(x)=\min}}. \quad (6)$$

For the potential (3), these frequencies are equal to $L^{-1}\sqrt{V_0/(2m)}$. In Figs. 2 and 3 we observe that this approximation satisfactorily reflects the dependence of the mobility peak position both on the period and on the modulation depth, even for intermediate modulation depths ($V_0 \geqslant 2k_BT$). This means that the major contribution to the oscillator peak is from carriers localized in the parabolic part of the potential.

Qualitatively same spectra are obtained for charges moving in the potential (4) (see Fig. 4). We now investigate the frequency of the oscillator peak as a function of the potential width α and steepness γ [Figs. 4 and 5]. There are two views of the charge motion in the potential well:

(1) If the bottom of the potential is flat and the walls are steep and high, charges will bounce between the walls and the oscillator frequency will be related to the average bouncing frequency $v_{\text{therm}}/(2w)$ (w is the width of the potential well and v_{therm} is the mean quadratic velocity $\sqrt{k_BT/m}$). Indeed, for potential (4) this behavior is observed for larger

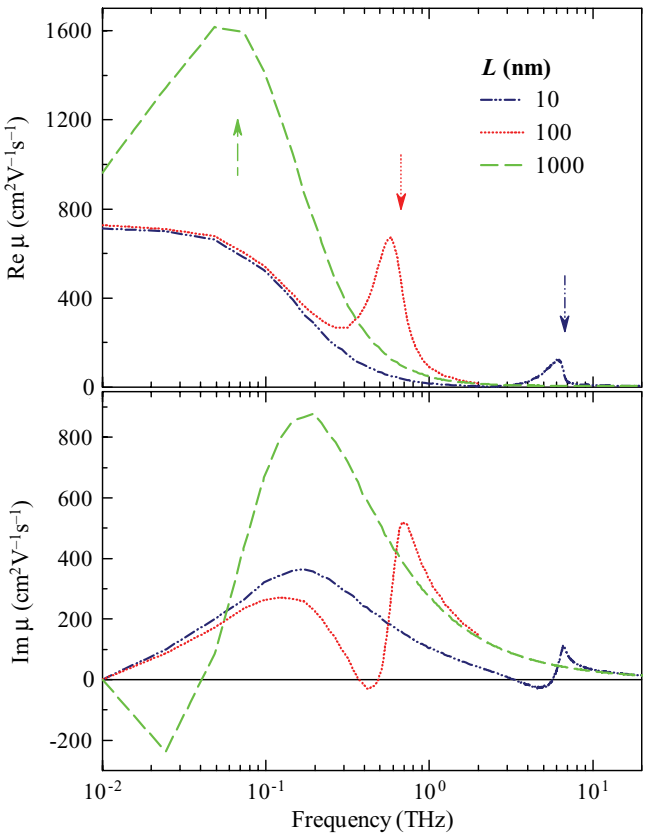

FIG. 3. (Color online) Real and imaginary parts of mobility spectra in potential (3) with constant depth ($V_0 = 2k_BT$) and with variable period (the spectra were calculated for $\tau_s = 1$ ps, $m = m_e$, and $T = 300$ K). The arrows indicate frequencies calculated using Eq. (6).

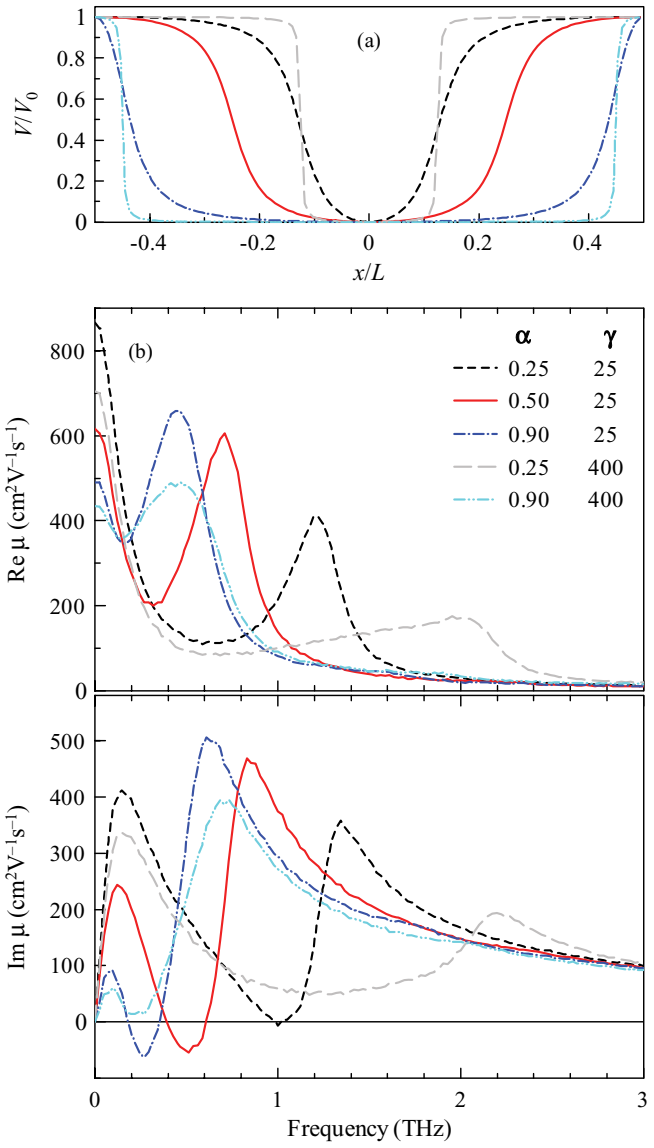

FIG. 4. (Color online) (a) Profiles of the potential (4) with various relative widths α and steepnesses γ. (b) Real and imaginary parts of mobility spectra in potentials from panel (a). The spectra were calculated for $V_0 = 2k_BT$, $L = 100$ nm, $\tau_s = 1$ ps, $m = m_e$, and $T = 300$ K.

widths α since the bottom is rather flat. In this regime, the frequency of the oscillator peak is insensitive to a further steepening of potential walls [see, e.g. spectra for $\alpha = 0.90$ in Fig. 4(b)].

(2) If charges remain only in the parabolic part of the potential well, the oscillator frequency will be described by Eq. (6). However, the potential (4) starts to be nonparabolic already for small displacements, i.e., Eq. (6) is an insufficient approximation of the oscillation frequency. Nonparabolic effects become more pronounced in combination with high wall steepness, giving rise to a markedly broadened oscillator peak [spectra for $\alpha = 0.25$ and $\gamma = 400$ in Fig. 4(b)].

These results demonstrate a clear relation between THz spectra and nanopatterning of semiconductors, which means that a careful analysis of measured THz spectra can bring valuable information of the nanolandscape of the potential energy in which charges move.

B. Response in magnetic field

The mobility of charges in a potential with hexagonal symmetry in a magnetic field is a tensor with two independent components:

$$\mu = \begin{pmatrix} \mu_{xx} & \mu_{xy} \\ -\mu_{xy} & \mu_{yy} \end{pmatrix}. \tag{7}$$

In such a situation, eigenmodes of electromagnetic radiation are circularly polarized and it is convenient to introduce the mobilities for left-handed and right-handed polarizations which read $\mu_- = \mu_{xx} + i\mu_{xy}$ and $\mu_+ = \mu_{xx} - i\mu_{xy}$, respectively. Since $\mu_-(f) = \mu_+^*(-f)$, the response to both circular polarizations is encoded in $\mu_-(f)$ with f including both negative and positive values.

The response of electrons moving in the potential (5) without the external magnetic field is the same as the response in the potential with one-dimensional modulation (Figs. 6 and 2, respectively)—it exhibits both Drude and oscillator peaks. Upon application of the magnetic field, the Drude model becomes[21]

$$\mu_\pm^{\text{Drude}} = \frac{e_0}{m} \frac{\tau_D}{1 - 2\pi i \tau_D (f \pm f_c)}, \tag{8}$$

which means that the Drude peak shifts in frequency and the resulting cyclotron motion has a resonant frequency

$$f_c = \frac{e_0 B}{2\pi m}. \tag{9}$$

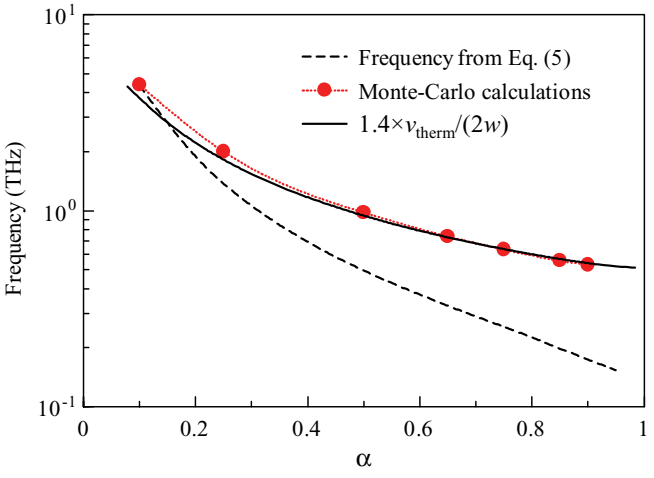

FIG. 5. (Color online) Frequency of the oscillator peak as a function of the relative width α of potential (4). Symbols: results of Monte Carlo calculations with parameters $V_0 = 6k_BT$, $L = 100$ nm, $\tau_s = 1$ ps, $m = m_e$, and $\gamma = 25$ (the dotted line is a guide for the eyes). Solid line: bouncing frequency $1.4 \times v_{\text{therm}}/(2w)$ approximates very well the oscillator peaks (w is the full width at half maximum of the potential; the factor 1.4 is empirical and it generally varies with the parameters of the potential—it accounts, namely, for the fact that not all carriers are reflected exactly at the half of the maximum of the potential). Dashed line: frequency calculated using Eq. (6) does not reproduce the α dependence of the oscillator peak frequency.

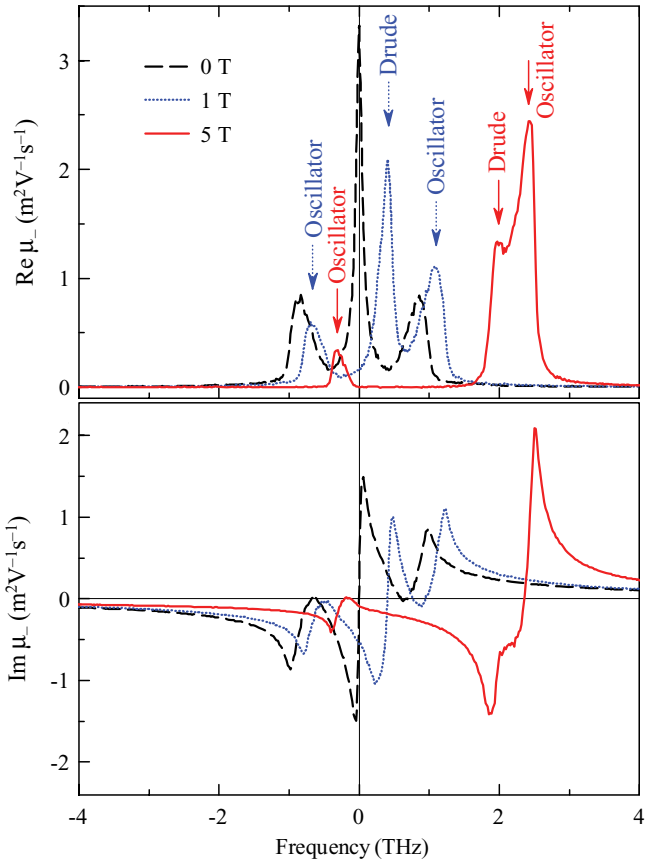

FIG. 6. (Color online) Real and imaginary parts of mobility spectra of negative charges moving in potential (5) for various magnetic fields. The spectra were calculated for $L = 100$ nm, $V_0 = 0.6 k_B T$, $m = 0.067 m_e$, $\tau_s = 3.8$ ps, and $T = 40$ K.

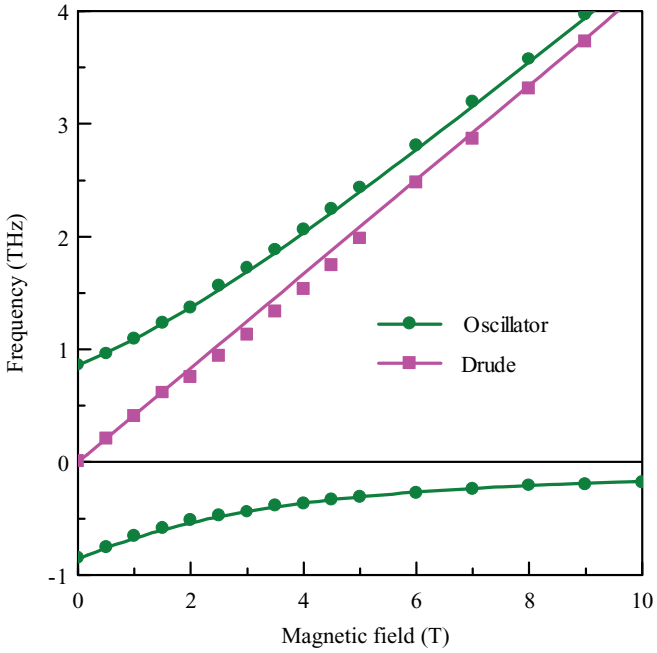

FIG. 7. (Color online) Symbols: frequencies of Drude and oscillator peaks in the real part of calculated mobility spectra (identical parameters as those in Fig. 6 were employed in the calculations). Lines: cyclotron frequency calculated from Eq. (9) and resonance frequency calculated from Eq. (11).

Indeed, exactly such a behavior is also observed for the Drude contribution in the presence of a modulated potential (Fig. 6); and also the peak frequency well coincides with the standard cyclotron resonance (Fig. 7) described by Eq. (9).

The behavior of the oscillator contribution with the magnetic field is more complicated and it can be understood based on the oscillations of charges in a parabolic potential. Their response in the magnetic field is described by

$$\mu_{\pm}^{\mathrm{osc}} = \frac{e_0}{2\pi m} \frac{if}{f^2 \mp f_c f - f_0^2 + if\Gamma/(2\pi)}, \qquad (10)$$

where f_0 is the oscillator frequency of the potential and Γ is the damping rate (see the Appendix). Consequently, there are two resonant frequencies in the spectrum of μ_{-}^{osc}:

$$f_{-}^{\mathrm{res}} = \frac{f_c \pm \sqrt{f_c^2 + 4 f_0^2}}{2}. \qquad (11)$$

If we now assign f_0 the value of the peak frequency obtained in our calculations without the magnetic field, Eq. (11) provides an excellent approximation of the evolution of oscillator peak frequency with magnetic field (Fig. 7). This behavior qualitatively reproduces the positions of resonances observed experimentally in a two-dimensional electron gas moving in a potential periodically modulated on the nanoscale.[18]

In a strictly parabolic potential, Eq. (10) predicts that the amplitudes of the oscillator peaks for opposite circular polarizations should be identical. Such a behavior is also observed in the potential (5) with deep modulation when nonparabolic effects are marginal. On the other hand, the peak amplitudes become markedly different for shallower modulations such as illustrated in Fig. 6. The circular-like motion of charges at frequencies corresponding to the oscillator peak for the left-handed polarization is very similar to the circular motion of free charges oscillating with cyclotron frequency, i.e., the charges are only weakly influenced by the potential modulation. This naturally suppresses the motion of charges in the opposite direction. As a result, the oscillator peak for the right-handed polarization becomes suppressed with increasing magnetic field while the oscillator peak for the left-handed polarization is enhanced.

IV. DEPOLARIZATION FIELDS

The qualitative role of depolarization fields can be straightforwardly understood in one-dimensional systems. In this case, the displacement D is constant, whereas the electric field intensity $E(x) = D/\varepsilon(x)$, where $\varepsilon(x)$ is the spatial profile of the (complex) permittivity. The effective permittivity $\varepsilon_{\mathrm{eff}}$ is then defined as the ratio of the displacement and electric field intensity averaged over a distance smaller than the wavelength, but much larger than the characteristic dimension of the pattern. In one dimension, the effective permittivity has a

particularly simple form:

$$\varepsilon_{\text{eff}} = \frac{\langle D \rangle}{\langle E \rangle} = \left\langle \frac{1}{\varepsilon} \right\rangle^{-1}, \tag{12}$$

which can be viewed as a connection of capacitors in series (the $\langle \ldots \rangle$ denotes a spatial average here). We express the local permittivity ε as a sum of a constant contribution ε_b due to lattice vibrations and another part due to conduction processes:

$$\varepsilon(x,f) = \varepsilon_b + \frac{i\sigma(x,f)}{2\pi f \varepsilon_0}, \tag{13}$$

where ε_0 is the permittivity of vacuum. The effective permittivity can be decomposed similarly:

$$\varepsilon_{\text{eff}}(f) = \varepsilon_{\text{eff},b} + \frac{i\sigma_{\text{eff}}(f)}{2\pi f \varepsilon_0}, \tag{14}$$

which thus defines the effective conductivity σ_{eff}:

$$\sigma_{\text{eff}}(f) = -2\pi i f \varepsilon_0 \left[\left\langle \frac{1}{\varepsilon_b + \frac{i\sigma(x,f)}{2\pi f \varepsilon_0}} \right\rangle^{-1} - \varepsilon_b \right]. \tag{15}$$

There are two important limits of this expression. For very weak local conductivity ($|\sigma(x)| \ll |2\pi f \varepsilon_0 \varepsilon_b|$ for all x), the effective conductivity is simply equal to an average local conductivity $\langle \sigma(x) \rangle$. This limit is very similar to that found in the case of Maxwell-Garnett approximation both for the case of conducting inclusions and conduction matrix (both nonpercolated and nonpercolated conductor, respectively).[4] Conversely, for very high local conductivity ($|\sigma(x)| \gg |2\pi f \varepsilon_0 \varepsilon_b|$ for all x) the background permittivity ε_b is negligible and the effective conductivity is equal to $\langle 1/\sigma(x) \rangle^{-1}$, which implies that the effective conductivity is limited by areas with the lowest local conductivity.

The intermediate cases as well as these limits are best illustrated by numerical calculations. For this purpose, we factorize the (local) conductivity as

$$\sigma(x,f) = n(x) e_0 \mu(f), \tag{16}$$

which means that its spectrum is determined by the spectrum of mobility while its spatial profile is controlled solely by local carrier density profile. Both these quantities are obtained from the Monte Carlo simulations described earlier. The additional parameter which can now be varied is the average carrier density $n_{\text{exc}} = \langle n(x) \rangle$. In Fig. 8, we see that for low carrier densities, the effective conductivity is indeed equal to the local conductivity. With increasing carrier density, the conductivity peak splits and one of the branches blueshifts. Such a behavior (plasmonic resonance) was already reported before and is related to the restoring force induced by separation of confined charges.[4,5] For the highest carrier densities, the plasmonic resonance broadens and shifts very high in frequency. However, the original conductivity spectrum persists with attenuated amplitude. Such a behavior is apparent when substituting Eq. (16) into $\langle 1/\sigma(x) \rangle^{-1}$: The spectral shape is preserved and the amplitude is limited by places with reduced carrier density $n(x)$. Note that this part of the spectrum may be very weak for confined carriers, due to the presence of areas with very low carrier density (right panel in Fig. 8).

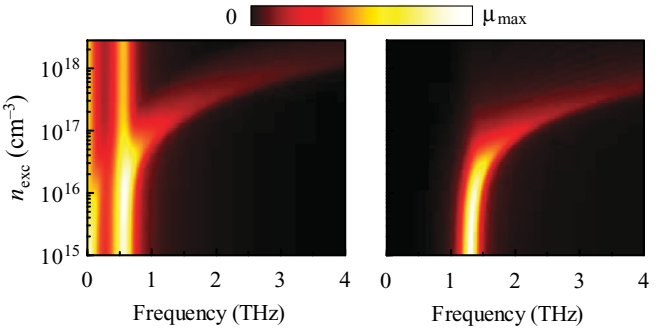

FIG. 8. (Color online) Spectra of the real part of the effective conductivity normalized by charge density [$\text{Re}\,\sigma_{\text{eff}}/(e_0 n_{\text{exc}})$] of charges moving in potential (3) with various depths. The spectra were calculated with the same parameters as in Fig. 1 and with $\varepsilon_b = 12$. Left panel: $V_0 = 2k_B T$, $\mu_{\max} = 680\,\text{cm}^2\,\text{V}^{-1}\,\text{s}^{-1}$; right panel: $V_0 = 8k_B T$, $\mu_{\max} = 1300\,\text{cm}^2\,\text{V}^{-1}\,\text{s}^{-1}$.

It should be noted that here we investigate systems with well-defined profiles of the permittivity and conductivity which allows one to exactly evaluate the role of the depolarization fields. Although there are some similar characteristics to those in the Maxwell-Garnett or Bruggemann effective medium approximations,[4] the assumptions of these approximations are not generally fulfilled, therefore these models are not applicable in our case.

V. CONCLUSIONS

In summary, we employed the Monte Carlo method to calculate terahertz conductivity spectra of charge carriers moving in a potential periodically modulated on the nanoscale. The spectra exhibit two characteristic features: a Drude peak owing to charge carriers with kinetic energy exceeding the modulation depth, and an oscillator peak due to charge carriers localized around potential minima. Both peaks exist for intermediate modulation depths, comparable with mean thermal energy $k_B T$. Shallow modulation depth favors the Drude peak, while deep modulation gives rise to the oscillator peak. Although the oscillator frequency can be estimated in some specific cases (flat or parabolic bottom of potential wells), it generally depends on the details of the potential energy landscape. Application of a magnetic field shifts the peaks—the shifts can be accurately predicted based on simple models of free charge carriers (cyclotron resonance) or of charge carriers localized in a parabolic potential. However, the distribution of oscillator strengths with a magnetic field depends on the detailed profile of the potential. Depolarization fields generally play an essential role when relating the calculated local conductivity spectra to the measured ones. Particular attention must be paid to their influence on the spectra when systems with strong localization and/or with high carrier densities are investigated. All these results extend the basis allowing the interpretation of THz conductivity spectra, which can be efficiently measured, e.g., by time-resolved THz spectroscopy.

ACKNOWLEDGMENT

This work was supported by Academy of Sciences of the Czech Republic (projects M100101218 and Open Science II).

APPENDIX: MOBILITY OF CHARGES IN A PARABOLIC POTENTIAL IN MAGNETIC FIELD

The equation of electron motion in a static magnetic field $\mathbf{B} = (0,0,B)$ reads as

$$m\frac{d^2\mathbf{x}}{dt^2} + m\Gamma\frac{d\mathbf{x}}{dt} + m\omega_0^2\mathbf{x} = -e\mathbf{E} - e\frac{d\mathbf{x}}{dt} \times \mathbf{B}. \quad \text{(A1)}$$

Considering only the two-dimensional motion in plane normal to $\mathbf{B}$, i.e., $\mathbf{x} = (x,y,0)$, we obtain after Fourier transformation

$$\begin{aligned} -\omega^2 x - i\omega\Gamma x + \omega_0^2 x &= -\frac{e}{m}E_x + i\omega\omega_c y, \\ -\omega^2 y - i\omega\Gamma y + \omega_0^2 y &= -\frac{e}{m}E_y - i\omega\omega_c x. \end{aligned} \quad \text{(A2)}$$

Solution for x and y then provides the components of the mobility tensor (7)—for example, the component μ_{xy} is defined as

$$\mu_{xy} = \frac{v_x(E_x = 0, E_y)}{E_y} = -i\omega\frac{x(E_x = 0, E_y)}{E_y}. \quad \text{(A3)}$$

Substitution into $\mu_\pm = \mu_{xx} \mp i\mu_{xy}$ then directly leads to Eq. (10). For the sake of brevity, $\omega = 2\pi f$.

*nemec@fzu.cz

[1] D. Grischkowsky, S. Keiding, M. van Exter, and C. Fattinger, J. Opt. Soc. Am. B **7**, 2006 (1990).

[2] T.-I. Jeon and D. Grischkowsky, Phys. Rev. Lett. **78**, 1106 (1997).

[3] M. C. Beard, G. M. Turner, and C. A. Schmuttenmaer, Phys. Rev. B **62**, 15764 (2000).

[4] H. Němec, P. Kužel, and V. Sundström, J. Photochem. Photobiol., A **215**, 123 (2010).

[5] H.-K. Nienhuys and V. Sundström, Appl. Phys. Lett. **87**, 2101 (2005).

[6] H. Němec, P. Kužel, and V. Sundström, Phys. Rev. B **79**, 115309 (2009).

[7] G. M. Turner, M. C. Beard, and C. A. Schmuttenmaer, J. Phys. Chem. B **106**, 11716 (2002).

[8] M. C. Beard, G. M. Turner, J. E. Murphy, O. I. Micic, M. C. Hanna, A. J. Nozik, and C. A. Schmuttenmaer, Nano Lett. **3**, 1695 (2003).

[9] D. G. Cooke, A. N. MacDonald, A. Hryciw, J. Wang, Q. Li, A. Meldrum, and F. A. Hegmann, Phys. Rev. B **73**, 193311 (2006).

[10] H. Ahn, Y.-P. Ku, Y.-C. Wang, C.-H. Chuang, S. Gwo, and C.-L. Pan, Appl. Phys. Lett. **91**, 3105 (2007).

[11] N. V. Smith, Phys. Rev. B **64**, 155106 (2001).

[12] H. Němec, P. Kužel, F. Kadlec, D. Fattakhova-Rohlfing, J. Szeifert, T. Bein, V. Kalousek, and J. Rathouský, Appl. Phys. Lett. **96**, 062103 (2010).

[13] Z. Mics, H. Němec, I. Rychetský, P. Kužel, P. Formánek, P. Malý, and P. Němec, Phys. Rev. B **83**, 155326 (2011).

[14] C.-H. Park and S. G. Louie, Nano Lett. **9**, 1793 (2009).

[15] R. Ulbricht, E. Hendry, J. Shan, T. F. Heinz, and M. Bonn, Rev. Mod. Phys. **83**, 543 (2011).

[16] H. Němec, J. Rochford, O. Taratula, E. Galoppini, P. Kužel, T. Polívka, A. Yartsev, and V. Sundström, Phys. Rev. Lett. **104**, 197401 (2010).

[17] R. Kubo, J. Phys. Soc. Jpn. **12**, 570 (1957).

[18] L. Nádvorník, M. Orlita, N. A. Goncharuk, L. Smrčka, V. Novák, V. Jurka, K. Hruška, Z. Výborný, Z. R. Wasilewski, M. Potemski, and K. Výborný, New J. Phys. **14**, 053002 (2012).

[19] N. Prodanović, N. Vukmirović, D. Indjin, Z. Ikonić, and P. Harrison, J. Appl. Phys. **111**, 073110 (2012).

[20] F. A. Hegmann, O. Ostroverkhova, and D. G. Cooke, *Photophysics of Molecular Materials* (Wiley-VCH Verlag GmbH & Co. KGaA, Weinheim, 2006), Chap. 7, pp. 367–428.

[21] E. D. Palik and J. K. Furdyna, Rep. Prog. Phys. **33**, 1193 (1970).